HAL
open science

Tomographic PIV calibration procedure in confined optical engine geometry

Petra Daher, Corine Lacour, Franck Lefebvre, Carole Gobin, Bertrand Lecordier

To cite this version:

Petra Daher, Corine Lacour, Franck Lefebvre, Carole Gobin, Bertrand Lecordier. Tomographic PIV calibration procedure in confined optical engine geometry. 13th International Symposium on Particle Image Velocimetry, Jul 2019, Munich, Germany. hal-02262353

HAL Id: hal-02262353

https://hal.science/hal-02262353v1

Submitted on 2 Aug 2019

HAL is a multi-disciplinary open access archive for the deposit and dissemination of scientific research documents, whether they are published or not. The documents may come from teaching and research institutions in France or abroad, or from public or private research centers.

L'archive ouverte pluridisciplinaire **HAL**, est destinée au dépôt et à la diffusion de documents scientifiques de niveau recherche, publiés ou non, émanant des établissements d'enseignement et de recherche français ou étrangers, des laboratoires publics ou privés.

13th International Symposium on Particle Image Velocimetry – ISPIV 2019
Munich, Germany, July 22-24, 2019

Tomographic PIV calibration procedure in confined optical engine geometry

Petra Daher, Corine Lacour, Franck Lefebvre, Carole Gobin, Bertrand Lecordier*

Normandie University, UNIROUEN, INSA ROUEN, CNRS, CORIA, 76000 Rouen, France

* bertrand.lecordier@coria.fr

Abstract

Tomographic PIV measurements require calibration accuracies of a fraction of a voxel throughout the entire investigation volume in order to provide reliable 3D data. This can be achieved today in a variety of applications by combining multiple planar recordings of a calibration target across the volume with the established self-calibration technique. However, when the considered application faces high confinement and severe optical deformations, obtaining an accurate calibration becomes difficult to achieve. A novel *ex-situ* calibration procedure is developed to overcome confinement and compensate optical deformation. The proposed approach establishes the correspondence between an originally confined investigation volume and its mapping function computed in the absence of confinement. The described *ex-situ* process is evaluated for the in-cylinder aerodynamics of an internal combustion engine. A particular pyramidal configuration of the tomographic recording system is employed. The in-cylinder flow is first computed via a classical *in-situ* calibration procedure obtained from an additional adjacent setup allowing free access into the engine's combustion chamber. Results are then discussed for multiple investigation volume thicknesses which is a critical parameter for 3D measurements. Finally, velocity fields obtained from the *ex-situ* procedure are compared to those ensuing from the *in-situ* calibration showing that the proposed approach is able to provide faithful camera models for volumetric reconstruction of confined flows.

1 Introduction

The behaviour of the turbulent flow during the intake and compression phases in the cylinder of an internal combustion engine strongly influences the air/fuel mixing processes and subsequently the combustion efficiency Buschbeck et al. (2012); Borée and Miles (2014). The different scales of the turbulent structures must be quantified and analysed in order to have a better understanding of the highly unsteady physical phenomena taking place in the combustion chamber of the engine. On the experimental investigation side, this is now conceivable with the simultaneous availability of high performance transparent optical engine and a wide range of laser diagnostics to investigate turbulent flow. In particular, the application of the tomographic PIV (TPIV) which offerts offers the 3 instantaneous velocity components of a flow in volume, becomes an unique approach to access the three-dimensional nature of the flow Elsinga et al. (2006); Peterson et al. (2017); Baum et al. (2013). However, TPIV requires a large optical access since it involves several cameras (usually 4) visualising the volume from different angles of view. These constraints complicate its application in engines where the combustion chamber has a confined geometry and limited optical access. Furthermore, a calibration target needs to be recorded across the volume in order to match viewing planes and obtain the conversion of the image space to an object space. However, when the experiment consists of a confined domain, moving a calibration target across the entire investigation volume becomes a challenging task J W A Martins et al. (2017). A second difficulty is related to the curvature and the thickness of the glass liner which induces strong deformations and

optical aberrations on the imaging systems, which are unusual for the TPIV approaches Daher et al. (2017); Daher (2018). To overcome geometric constraints and ensure the accuracy of data processing, an original *ex-situ* calibration technique has been developed. The proposed approach establishes the correspondence between an originally confined investigation volume and its mapping function computed in the absence of confinement. The combination of these two data makes it possible to obtain new camera models taking into account deformations. In a final step, these models are refined to reach a sub-voxel accuracy by a « *self-calibration* » procedure Wieneke (2008). Thus, the proposed *ex-situ* calibration technique is transferable to all configurations that faces the problems of confinement and restricted optical access. In order to validate our *ex-situ* model, the engine velocity fields are compared to those obtained from a conventional TPIV calibration *in-situ*. To conclude this paper and shows the potential of TPIV to investigate a such kind of flow, the first results of 3D measurement in the engine are presented.

2 Experimental setup and TPIV description

2.1 Experimental setup

The considered application to validate the *ex-situ* process is an AVL optical engine that provides an excellent example of a confined flow with severe optical deformations (figure 1). It allows visualising the engine's internal flow through its transparent cylinder while operating at rotational speeds up to 3000 *rpm*. Throughout the study, we'll be addressing the internal combustion engine's aerodynamics in motored conditions, i.e. without injection or firing. For that purpose, the spark plug is cut off and the injector is replaced with a fake one. In addition to its quartz cylinder, the engine offers the possibility to access the combustion chamber through a transparent quartz piston head under which is placed a 45° mirror. This mirror allows sending a laser sheet through the piston to form a vertical plane inside the cylinder therefore avoiding strong light reflexions that would occur if a laser sheet crossed the cylinder from side to side passing by a multi-curved glass interface. For the desired measurements of in-cylinder aerodynamics, the TPIV investigation volume is fixed by establishing a thick light sheet between the intake valves centred at the cylinder's symmetry plane z_0. Moreover, the light sheet thickness is controlled via knife-edge cutters fixed on micrometric translation plates placed between the cylindrical lens and the mirror, parallel to the laser sheet. The laser used is a double pulsed PIV Spectra Physics delivering 350 mJ per pulse while at 532 nm and 10 Hz. It is coupled to 4 Hamamatsu CCD cameras (C9300 - 4M pixels) equipped with PC-E Micro NIKKOR lenses (45mm f/2.8D) with Scheimpflug adapters for perspective control. As seen in figure 1(a), the engine's geometry limits the angles of view into the combustion chamber. Therefore, a compact pyramidal configuration of the recording system is chosen as shown in figure 1(b). This choice differs from previous studies Baum et al. (2013) on this kind of configuration and it allows to keep distinct angles of view in spite of an optical access strongly constrained by the geometry of the engine (figure 1(a)). This configuration ensures 4 independent angles of view ranging between 20 and 30 degrees with respect to the cylinder's axes. Finally, the achieved field of view has a resolution of 2048×2048 pixels corresponding to $81.81.\Delta_Z\ mm^3$, where Δ_Z is the volume thickness. During the test campaign, three volume thicknesses are considered, Δ_Z = 3, 5 and 8 mm respectively referred to as L3, L5 and L8 hereafter. For each case, 500 particle images are recorded for different crank-angles (250 velocity fields). In the present document, only a selected part of the test campaign results will be reported. The full database description and results can be found elsewhere in Daher (2018).

Furthermore, the quality of PIV measurements and the validity of data sets are highly dependent on the choice of seeding particles and seeding density. For this purpose, an in-house made aerosol generator allowed producing tracer particles of 1 to 5 µm diameter that faithfully follow the flow while ensuring good signal to noise ratio. The substance used is olive oil that is able to sustain high temperatures especially occurring during the compression stroke. Finally, in order to obtain phase-locked data, the desired angular position is extracted with a precision up to 0.1 crank angle degree via an AVL timing unit connected to the engine test bench. This reference pulse is dependent on the engine's rotational speed. The recording

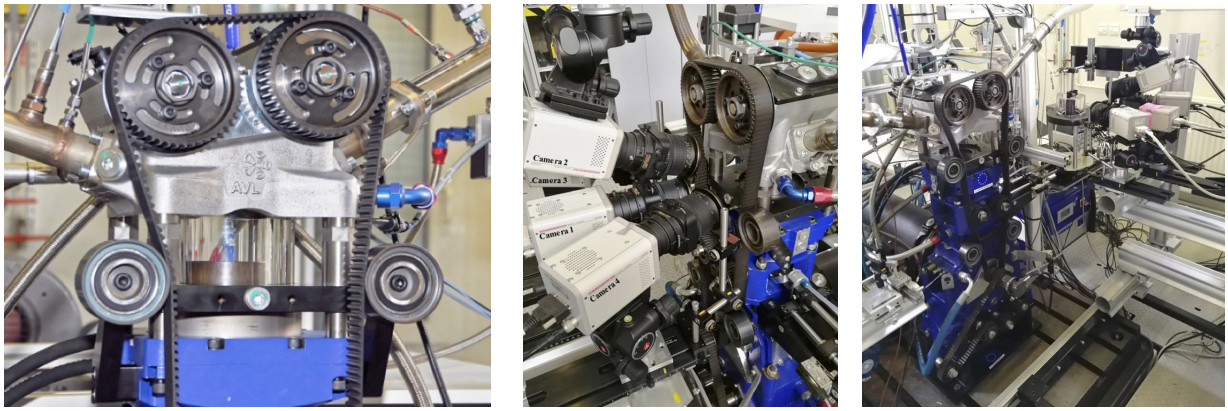

(a) Single cylinder optical engine (AVL) (b) Pyramidal TPIV configuration (c) TPIV configuration and in-situ calibration setup

Figure 1: Single cylinder optical engine, TPIV system and calibration setup

speed meanwhile is imposed by the cameras capacity. Therefore an authorisation pulse is introduced such as a recording sequence is triggered only when both reference and laser pulses coincide. In order to control this synchronisation process, all pulses are connected to an external programming unit that also allows adjusting the PIV frame separation time with respect to in-cylinder flow dynamics

2.2 3D velocity maps reconstruction

The volumetric reconstruction is performed by means of the simultaneous multiplicative algebraic reconstruction technique (SMART) with an initialisation method that includes a min-LOS first step. Two iterations with raytracing interaction method, a variable relaxation parameter and a volume-filter threshold of 0.001 are employed. In order to optimise the quality of particle images for PIV computations, an image pre-processing step is performed where a particle-free mean background image is computed for each laser pulse with respect to each of the 4 cameras and is then subtracted from all corresponding particle images. Then a division by a mean particle image is performed and a 3×3 Gaussian filter is applied. This significantly reduces the noise during image reconstruction. As a result, reconstructed particle volumes of $51.51.\Delta_Z\ mm^3$ are obtained with good back-projection quality exceeding 85% in all the cases. Velocity fields are then computed from pairs of volumes by means of normalised 3D cross-correlation with Gaussian sub-pixel peak interpolation method and a spline image interpolation method. The spatial resolution is similar between the different light sheet thicknesses. In the iterative calculation process, the final pass is done over an interrogation window size of 20.20.20 pixels corresponding to $0.83.0.83.0.83\ mm^3$ along to a 75% overlap factor. The codes used for computation are those developed by PPRIME institute (Thomas et al. (2014)). As a result, 250 velocity fields of 50×50×k vectors are obtained where k =12 for L3, 20 for L5 and 31 for L8.

3 Calibration

3.1 Introduction

The evaluation accuracy of camera model parameters (pinhole, Soloff, polynomial ...) is a crucial issue in the tomo PIV approach and much more critical than for stereoscopic PIV. It consists of moving a geometrically calibrated object (dot pattern, graph paper, etc.) into the measurement volume and extracting its characteristics on each camera image to determine the model parameters. For the final refinement of model characteristics, this step is usually

followed by a *"self-calibration"* procedure performed on very low concentration particle images (Wieneke (2008)).
This approach, well adapted to open and large configurations becomes often difficult to apply when the flow is confined and the dimensions of the experiment are reduced. In this work, we propose an original 3D calibration approach *ex-situ* which associates a calibration without confinement with a geometric transformation evaluated only in the central plane of the volume and allowing the passage of an imaging system with to without confinement. The combination of these two data makes it possible to obtain 3D models for the cameras, which take into account the optical deformations introduced by the presence of the confinement.

3.2 Principle of the 3D *ex-situ* calibration

The *ex-situ* calibration procedure is presented in Figure 2. The approach proposed here establishes the correspondence between an originally confined investigation volume and its mapping function computed in the absence of confinement. A full 3D calibration process is done in the absence of the optical window and is then associated to a single fixed calibration plane recorded at the central position of the confined investigation volume. The optical distortion introduced by the window is then compensated by the *ex-situ* calibration models obtained by performing four main steps:

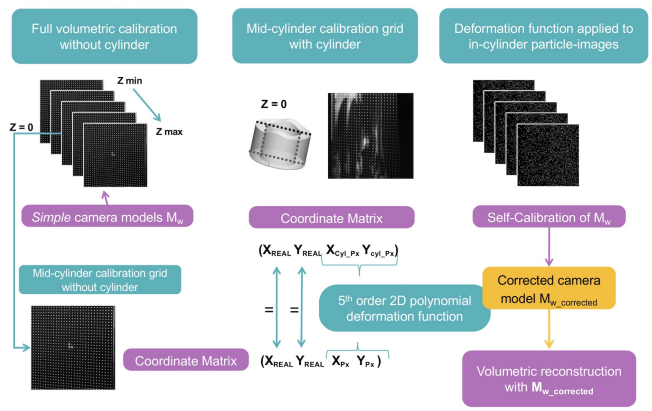

Figure 2: *ex-situ* calibration procedure

(1) The first step is recording the calibration target in multiple planes across the investigation volume in the absence of the optical window, i.e. confinement. A reference plane z_0 is used to identify the central plane of the investigation volume. The recorded targets are then used to extract grid coordinates at all considered Z-positions and compute the mapping function of each camera using adequate modelling such as pinhole, Soloff, polynomial or other.
(2) The second step is recording the calibration target at z_0 of the confined chamber, i.e. in the presence of the optical window. Then, a deformation function F_{def} is computed to describe the transformation between two grids: z_0 recorded in-window and z_0 recorded with no-window. Having the same calibration target in the same physical space, the correspondence between the two domains is obtained via a deformation function
(3) The deformation function F_{def} is then used to project low density particle images recorded in the original geometry on the newly defined no-window domain where z_0 grid deformations are taken into consideration and corrected.
(4) In a last step, a volumetric self-calibration is performed using the projected particle images of (3) to refine the ensuing camera models computed in (1), thus resulting in the ex-situ camera models that will be used for volumetric reconstruction of the new no-window domain. The latter is similarly obtained by projecting all recorded particle images using F_{def}. As a result, the *ex-situ* procedure allows overcoming confinement while reducing optical deformations which in turn highly impacts computation time since severe deformations usually necessitate high order camera models in order to be taken into account in flow reconstruction.

3.3 Accuracy assessment of the *ex-situ* calibration

In order to validate this procedure, a classical calibration referred to as *in-situ* calibration is simultaneously performed and their consequent volumetric reconstruction of in-cylinder measurements are compared. For this purpose and to obtain the required access into the combustion chamber, the recording system is installed on translation rails and shifted to a new position next to the engine test bench without compromising the cameras adjustments.

An additional setup is then mounted in order to mimic with precision the cylinder's position with respect to the cameras assembly (Figure 1(c)). In this new position, it is possible to freely move the calibration target across the whole investigation volume in the presence of the cylinder that in turn is easy to remove. A Soloff model for each of the four cameras is then evaluated before refining with a final step of *"self-calibration"* Wieneke (2008) using 250 recorded particle images at very low density.

First, the ensuing ensemble averaged velocity fields of 250 instantaneous measurements obtained at the Bottom Dead Center (BDC) are shown in Figure 3 where iso-surfaces reveal magnitudes of the velocity. This first result reveals identical flow characteristics for both calibration processes. In this representation, we do not observe the slightest divergence between the two approaches both in the amplitude of the velocities and in the positioning of the vortex structure present at this timing of the engine cycle Daher (2018). To try to distinguish more precisely the difference between the methods, in the figure 4. we present a cross section of the volume of the figure 4 in the plane $z = 0$ mm (*in-situ*: figure 4(a) - *ex-situ* : figure 4(b)) as well as speed profiles in $y = -5$ *mm* (figure 4(c)). As in the 3D representation of the figure 3, we do not see any noticeable difference between the two approaches. This confirms that our *ex-situ* calibration method gives results comparable on average to those of classical techniques.

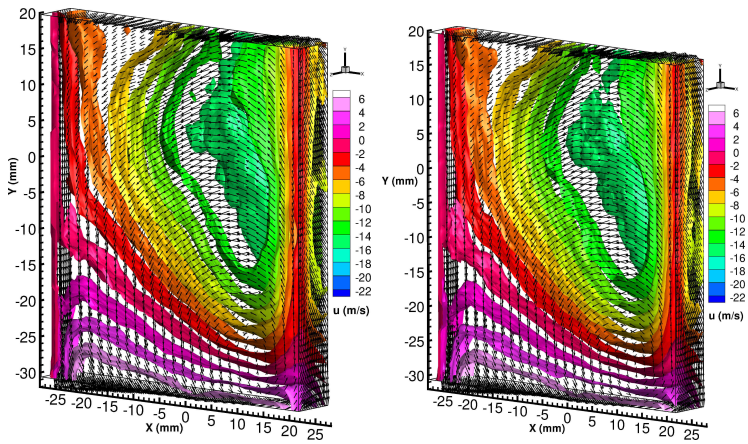

(a) *in-situ* calibration (b) *ex-situ* calibration

Figure 3: Comparison of ensemble average velocity field from *in-situ* (left) and *ex-situ* (right) (2000 rpm - case *L*8)

In order to go further in the comparison, in the figure 5 we present the correlations of the spatial averaged velocity (top) and fluctuations (bottom) for the two methods of calibration in the external plane ($z = -4mm$) of the volume. For velocity components u and v, very high correlations are observed and then it confirmes the reliability of our *ex-situ* calibration for the two main velocity components. For the w component, the comparison is more delicate due to a low velocity range in the plane of symmetry of the valves for this component. Nevertheless, a correlation between the results for the 2 calibration methods is still clearly observable.//

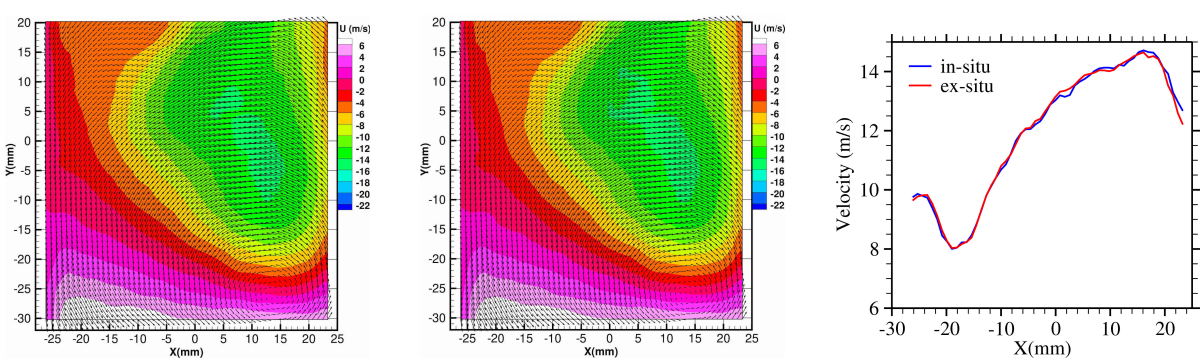

(a) *in-situ* calibration (b) *ex-situ* calibration (c) Profile comparaison

Figure 4: Cross section in the plane z_0 for both calibration for the velocity field of figure 3 and velocity profiles at $y = -5$ *mm*

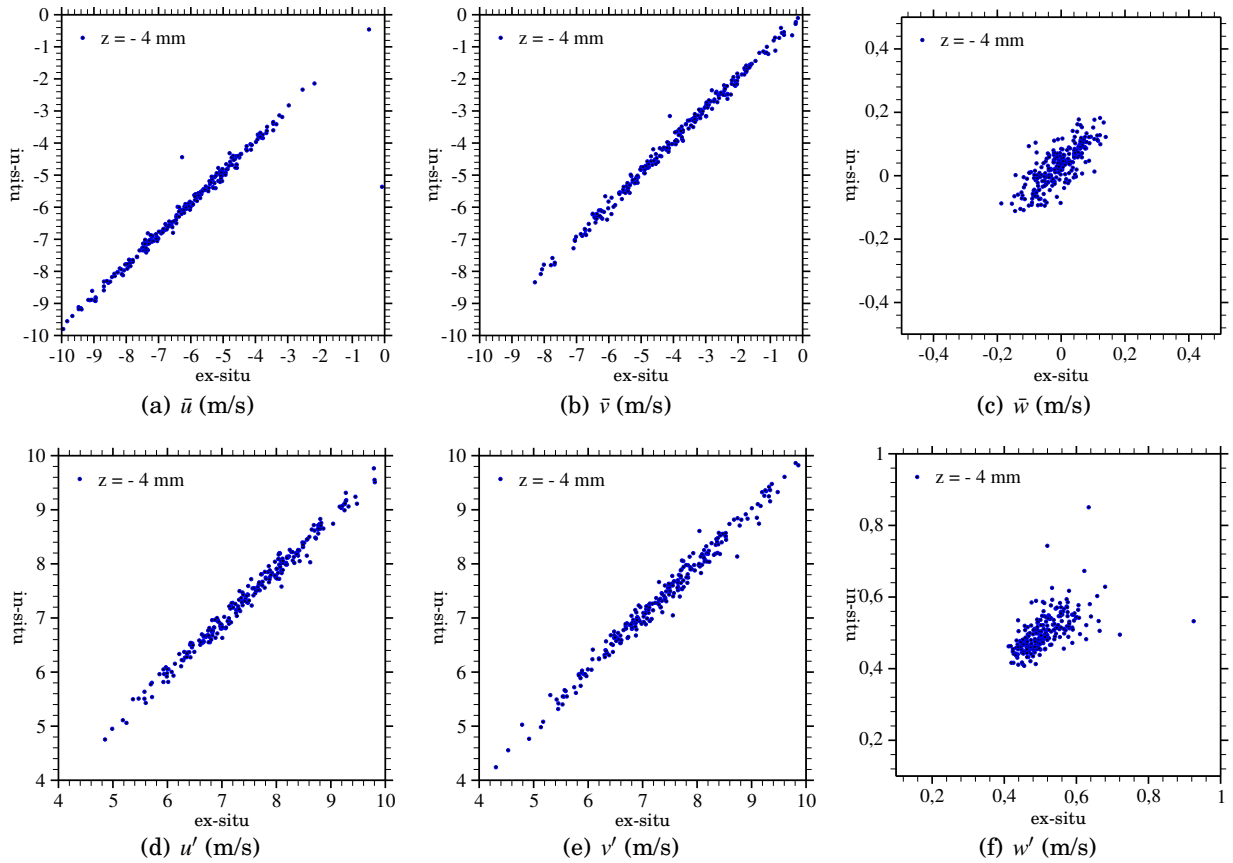

(a) $\bar{u}$ (m/s) (b) $\bar{v}$ (m/s) (c) $\bar{w}$ (m/s)

(d) u' (m/s) (e) v' (m/s) (f) w' (m/s)

Figure 5: Correlation of the three components of the average velocity for the two calibrations (a, b, c) and fluctuation (d, e, f) extracted in the plane $z = -4$ mm (case $L8$)

In conclusion of these different results, a perfect similarity between the two calibration approaches have been observed and thus validates our *ex-situ* method. A more detailed analysis of the comparison can be found elsewhere in reference Daher (2018).

4 Volume thickness optimisation

One of the important parameters in 3D velocity measurements is the thickness of the volume. In the majority of cases, it is delimited by the volume of illumination of the flow. The requirement to maintain particle concentrations below 0.1 *particle per pixel (ppp)* on images for high quality reconstruction requires a direct relationship between the thickness of the illumination domain and the concentration of seeding particles introduced into the flow. In our experience, the increase in distortion phenomena on the image sides can also lead to limit the maximum size of the volume of investigation. In order to maximise the thickness of volume without significantly reducing the quality and accuracy of the velocity field, we compared results obtained with different volume thicknesses (3, 5 and 8 *mm*), maintaining constant the particle image density by a fine adjustment of the seeding concentration. A higher volume thickness has not been considered because it required to design a complex optical arrangement to enlarge significantly the laser beam, while conserving a *"top hat"* profile favorable to the 3D reconstruction. In addition, the lower energy density induced by larger volumes led to a significant degradation of the signal-to-noise ratio of the particles images.

The first comparison was made on the averaged velocity fields (250 samples) reconstructed over the common areas of 3 *mm* for both cases L3 and L8 (Figure 7). The similarity between mean velocity magnitudes across the field of view are again revealed. The few observed dif-

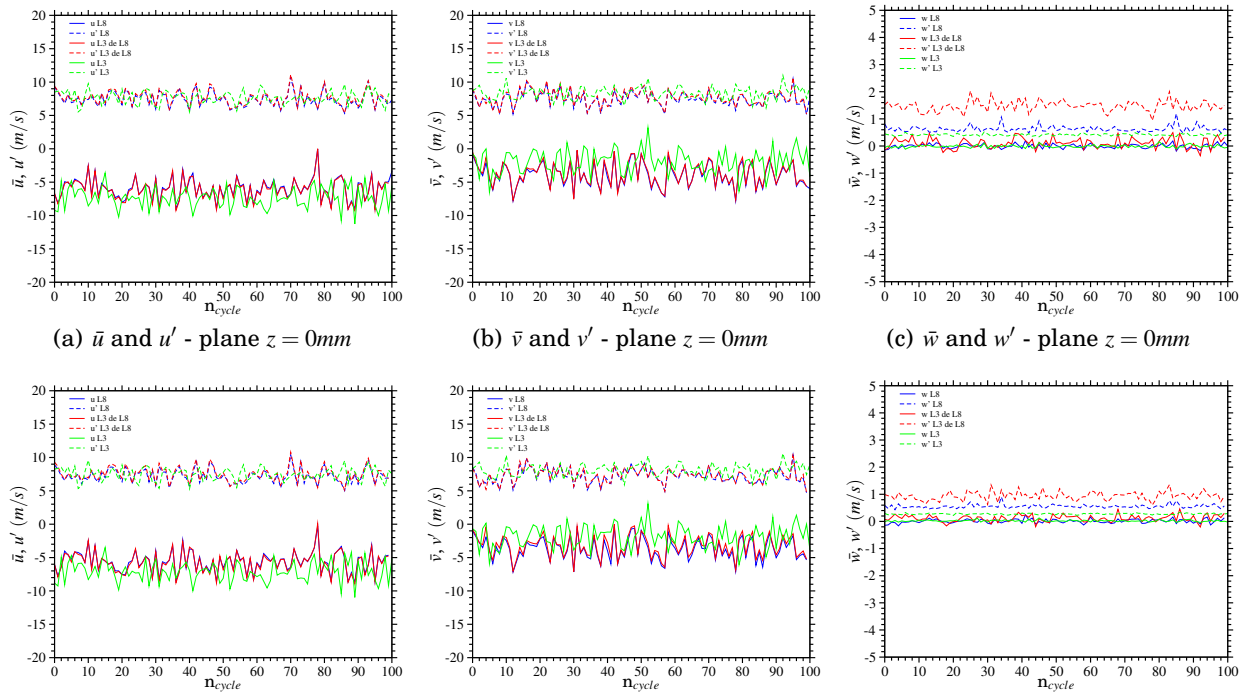

(a) $\bar{u}$ and u' - plane $z = 0mm$ (b) $\bar{v}$ and v' - plane $z = 0mm$ (c) $\bar{w}$ and w' - plane $z = 0mm$

(d) $\bar{u}$ and u' - plane $z = 1.5mm$ (e) $\bar{v}$ and v' - plane $z = 1.5mm$ (f) $\bar{w}$ and w' - plane $z = 1.5mm$

Figure 6: Comparaison of the velocity statistics (planes $z = 0$ et $z = 1.5mm$) for a reconstruction of cases L3 and L8 over a domain of 3 *mm*

ferences is believed to be a reflection of the separated time periods of measurements and the moderate number of recorded particle images (250) imposed by the short engine run time. This first result therefore shows that in a common reconstruction zone, velocity measurements are very close in average and that a thickness of 8 *mm* seems reasonably accessible for our study.

Hence in order to refine the comparison between the common areas of the 3 test campaigns, a statistical analysis is conducted over the 100 instantaneous velocity fields. The mid-cylinder plane as well as the boundary plane of the common region, i.e. Z=+1.5 mm, are extracted from all velocity fields and from the 2 volume thicknesses L3 and L8 reconstructed over 3 *mm*. On this graph, the case L8 reconstructed on the entire domain is also plotted. We can note that the acquisition been done at different times for cases L3 and L8, and in consequence it is not possible to compare the cycle-to-cycle

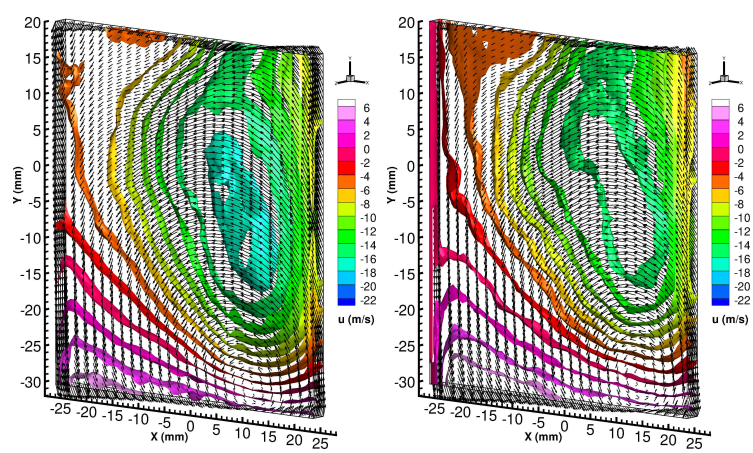

(a) Case (*L3*) (b) Case (*L8*)

Figure 7: L3 (left) and L8 (right) ensemble average velocity field reconstructed over 3 *mm*

results. For that reason, only the evolution of averages and fluctuations as well as the amplitude of their variations can be compared.
Figure 6 shows the variations of $\bar{u}$ and u' magnitudes for the 250 planes revealing thus a similar range between L3 and L8 data sets with a slight shift of the latter. In addition to the data sets being recorded at different time periods, this shift can be caused by the increased smoothing in volumetric reconstruction of L8 that was required to obtain similar reconstruction quality as the other cases. For the results in the central plane of the volumes (Figures 6(a), 6(b) et 6(c)), the average values of the three components have identical ranges of variation. This confirms the very good similarity of the average fields observed in the figure 7. For the velocity fluctuations u' (Figure 6(a)) and v' (Figure 6(b)), we also observe very similar results and no amplification or attenuation of the fluctuations of case L8 which could indicate an increase of noise or a smoothing of the velocity fields in compared with the case L3. In contrast, for the w component, a slight increase in the fluctuation is observed (Figure 6(c)) for the case L8 compared to the case L3. For case L8 reconstructed over the entire volume, the increase of w' can be explained by an estimation of w' obtained over a larger volume, taking into account the strong 3D flow behaviour of the flow which is more pronounced than in the central plane. For the L8 case reconstructed over 3 mm, the increase of w' is more difficult to explain. We think that it is induced by an increase of ghost particle in the reconstruction due to the restriction of the reconstruction domain to 3 mm, whereas the particles images are recorded with a physical volume thickness 8 mm.
From this analysis, we can conclude that in our experimental conditions, the use of a volume with a thickness of 8 mm provides robust results over the entire domain without affecting the quality of the results compared to thiner volumes. For the rest of the study, this volume thickness has been adopted.

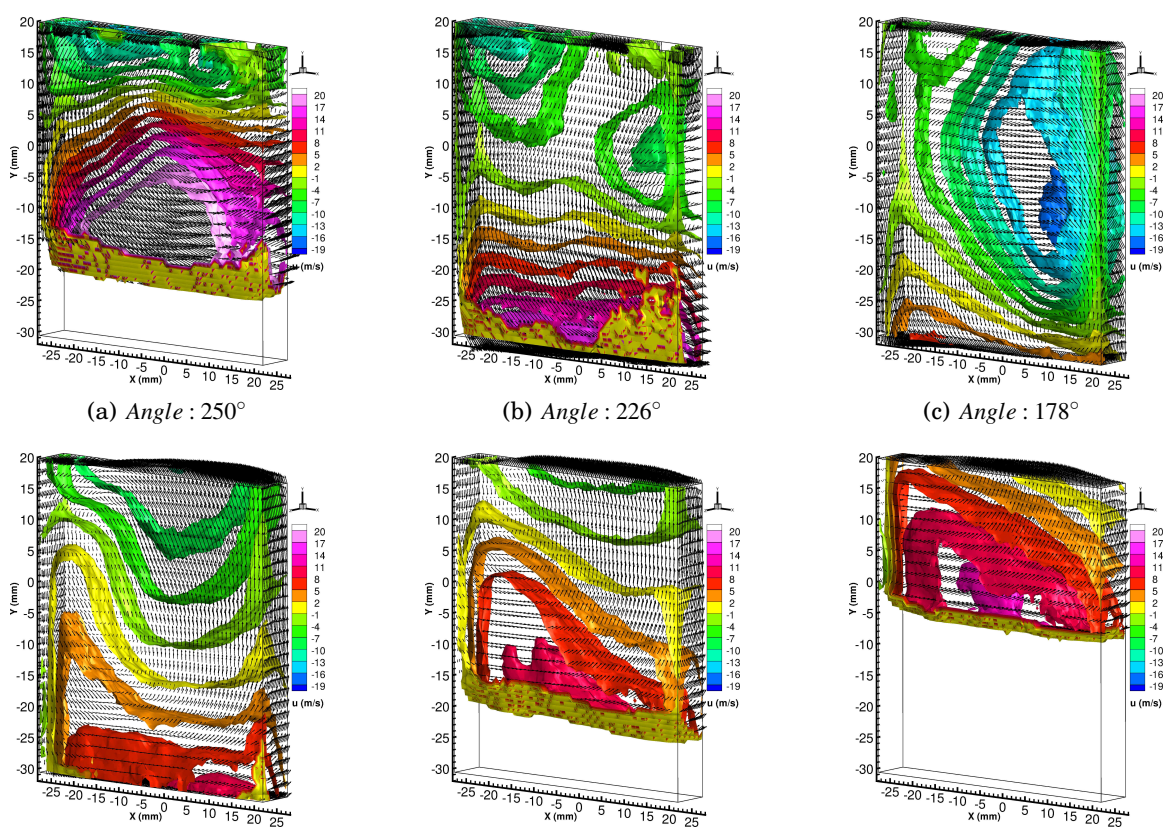

(a) *Angle* : 250° (b) *Angle* : 226° (c) *Angle* : 178°

(d) *Angle* : 130° (e) *Angle* : 106° (f) *Angle* : 82°

Figure 8: Ensemble average velocity field (250 samples) and iso-surface of u (case L8, 2000 tr/min, $P_{ad} = 1$ bar) during both admission (250°, 226° et 178°) and compression (130°, 106° et 82°) phases

5 Preliminary results

In the Figure 8, a series of average velocity field computed from 250 instantaneous 3D fields recorded at 6 crank angles during both admission and compression phases are presented. All these results correspond to engine operating conditions equal to 2000 *rpm* and an intake pressure of 1 *bar*. During the intake phase, the formation of a large turbulent structure (tumbling motion) characteristic of aerodynamics in gasoline spark ignition engines is observed Baum et al. (2013); Daher (2018). For the last two crank-angles, an acceleration of the rotation of the vortex structure occurs just before breaking towards the smallest turbulence scales at the end of compression before ignition. For these 6 crank angles, these average results are in agreement with those obtained by low frequency PIV and time resolved PIV in the central plane $z0$ with the same conditionsDaher (2018). This observation allows in a first step to validate the 3D measurements in the engine before in a second time to carry out more advanced analyses taking into account the strongly 3D and unsteady characters of the in-cylinder flow. Indeed, in the present paper, the potential of instantaneous 3D velocity fields has not yet been fully exploited but they open a wide range of potentialities to investigate the strong 3D unsteady character of in-cylinder flow and the cycle-to-cycle variations. These aspects will be investigated in term of variability of the position and orientation of the tumbling motion as well as energy fluctuation.

6 Conclusions et perspectives

In this work, an application of the tomographic PIV technique in the case of a spark ignition engine is proposed to analyse the 3D character of in-cylinder flow in realistic operating conditions. The use of this optical method in a confined environment with limited optical access remains delicate, in particular for the 3D calibration step. Therefore, a new approach of calibration *ex-situ* has been proposed which consists of performing a 3D calibration in the absence of confinement in parallel with a measurement of the optical deformations introduced in the central plane z_0 of the volume. This new approach of calibration has been compared successfully with the conventional one and it allows to faithfully reveal the flow's characteristics with less than 2.5% error across the whole volume. As a conclusion, the ex-situ process allowed overcoming the confinement of the chamber while minimising optical deformations and optimising the cost of the experimental procedure with no additional setups required. Our original approach is applicable in all configurations where it is difficult to move freely a calibration target throughout the investigation domain.

Next to the validation of the *ex-situ* calibration procedure, the acquisition parameters have been optimised and in particular the thickness of the measurement volume, which in our case reach up to 8 *mm* without introducing significant biais. The first results of the 3D averaged velocity fields were presented for several crank angles and it showed all the potentials of the tomographic PIV to investigate a such complex unsteady 3D flow. For further study of the in-cylinder flow, we will have to analyse the 3D instantaneous fields to try to evaluate the influence of the instabilities of the jets valve on cycle-to-cycle variations, data difficult to access from a 2D-2C or 2D-3C PIV techniques.

Acknowledgements

This work was conducted as part of the ESSENCYELE project (moteur ESSENCe injection directe hYbride Electrique abordabLE), funded by the Agence De l'Environnement et de la Maîtrise de l'Energie (ADEME France).

References

Baum E, Peterson B, Surmann C, Michaelis D, Böhm B, and Dreizler A (2013) Investigation of the 3d flow field in an ic engine using tomographic piv. *Proceedings of the Combustion Institute* 34:2903 – 2910

Borée J and Miles PC (2014) *In-cylinder Flow*. pages 1–31. American Cancer Society

Buschbeck M, Bittner N, Halfmann T, and Arndt S (2012) Dependence of combustion dynamics in a gasoline engine upon the in-cylinder flow field, determined by high-speed piv. *Experiments in fluids* 53:1701–1712

Daher P (2018) *Spatiotemporal analysis of coherent structures in confined environments via time-resolved and tomographic PIV : case of internal combustion engine aerodynamics*. Ph.D. thesis. Normandie University

Daher P, Lacour C, Lefebre F, Cessou A, Tremblais B, Thomas L, David L, and Lecordier B (2017) Novel ex-situ calibration procedure for tomographic piv in a confined environment: Application to a single-cylinder optical engine. in *The 12th International Symposium on Particle Image Velocimetry – ISPIV At: Busan, Korea*

Elsinga GE, Scarano F, Wieneke B, and van Oudheusden BW (2006) Tomographic particle image velocimetry. *Experiments in Fluids* V41:933–947

J W A Martins F, Foucaut JM, Stanislas M, and Azevedo L (2017) Tomo-piv of turbulent water flow in a square duct employing external calibration. in *The 12th International Symposium on Particle Image Velocimetry – ISPIV At: Busan, Korea*

Peterson B, Baum E, Ding CP, Michaelis D, Dreizler A, and Böhm B (2017) Assessment and application of tomographic piv for the spray-induced flow in an ic engine. *Proceedings of the Combustion Institute* 36:3467 – 3475

Thomas L, Tremblais B, and David L (2014) Optimization of the volume reconstruction for classical tomo-piv algorithms (mart, bimart and smart): synthetic and experimental studies. *Measurement Science and Technology* 25:035303

Wieneke B (2008) Volume self-calibration for 3d particle image velocimetry. *Experiments in Fluids* 45:549–556